INSTITUTE OF PHYSICS PUBLISHING SEMICONDUCTOR SCIENCE AND TECHNOLOGY

Semicond. Sci. Technol. **21** (2006) 320–334 doi:10.1088/0268-1242/21/3/021

Two-beam cross-modulation photocarrier radiometry: principles and contrast amplification in semiconductor subsurface imaging

Derrick Shaughnessy, Andreas Mandelis, Jerias Batista[1], Jordan Tolev and Bincheng Li

Center for Advanced Diffusion-Wave Technologies (CADIFT), Department of Mechanical and Industrial Engineering, University of Toronto, Toronto M5S 3G8, Canada

E-mail: mandelis@mie.utoronto.ca

Received 4 August 2005, in final form 9 December 2005
Published 1 February 2006
Online at stacks.iop.org/SST/21/320

Abstract

A two-beam photo-carrier radiometry (PCR) technique of semiconductors has been developed. The technique operates on the superposition of superband-gap and subband-gap laser beams which results in the cross-modulation of the backscattered subband-gap laser intensity by the harmonically varying free-carrier-wave density-dependent infrared absorption coefficient. A theory of this two-beam cross-modulation approach and various experimental configurations applied to the imaging of electronic contamination and defects in silicon wafers are presented. Owing to the nonlinear interaction of the two beams, the configuration revealed a new optoelectronic effect, the decrease of the residual subband-gap absorption coefficient due to the decreased carrier capture cross-section brought about by the depletion of occupied band-gap states in the presence of photons produced by radiative recombination. Quantitative values of the optoelectronic constant B associated with the rate of depletion of free-carrier capture cross-section with superband-gap intensity, as well as of I_{eR}, the intensity of radiative recombination emissions, were obtained. These values cannot be measured by conventional PCR or other single-ended optoelectronic techniques. The theory explains the experimental dependence of electronic transport properties on the intensity of the subband-gap beam and accounts for optoelectronic imaging contrast amplification in contaminated or defect semiconductors. The two-beam cross-modulation PCR was further shown to enhance the imaging contrast of a certain electronic contamination type (Fe in p-Si). A dramatic phase contrast enhancement of subsurface defects made by low-dose proton implantation was demonstrated at superband-gap laser intensity levels one order of magnitude lower than possible with single-ended optoelectronic imaging methodologies. This is tentatively attributed to relatively low-injection trap-filling well below optoelectronic trap saturation.

1. Introduction

Optical absorption processes in semiconductors generally result in the excitation of an electron from a lower- to a

[1] On leave from: Departamento de Física, Universidade Federal do Maranhão, Av dos Portugueses, s/n, 65085-580 São Luís, MA, Brazil.

higher-energy state, although photons can be coupled directly to the vibrational modes of the lattice or impurities. Fundamental absorption which is accompanied by the promotion of an electron from the valence band to the conduction band is the dominant process for photon energies greater than the band gap (wavelengths less than $\sim$1.1 μm in silicon). Although silicon is nearly transparent in the near to far IR, transitions do exist that allow for absorption processes at photon energies below the band gap. The most dominant of these mechanisms is attributed to free carriers that are able to make transitions to higher energy levels within their respective energy bands through the absorption of a photon with subband-gap energy (near-IR and longer for silicon). Intra-band absorption-induced energy transitions require a change in momentum larger than that of the absorbed photon and thus must involve a scattering event with a lattice phonon or an impurity. Scattering by acoustic phonons leads to a $\lambda^{1.5}$ dependence [1]; by optical phonons leads to a $\lambda^{2.5}$ dependence [2]; and by ionized impurities to a $\lambda^{3.0}$ to $\lambda^{3.5}$ dependence [3]. Here λ is the free space wavelength. In general, all of the scattering processes will be available and the dominant mode of scattering will depend on the impurity concentration. Regardless of the scattering mechanisms involved, the free carrier absorption spectrum is relatively featureless and monotonically increases as a function of wavelength and of the free carrier density [4, 5]. The classical description of an electron in the periodic electric field of the lattice is given by the Drude–Zener theory and predicts the following free carrier absorption coefficient [6],

$$\alpha(N;\lambda) = \frac{N\lambda^2 q^3}{4\pi^2 \in_0 m_c^* c^3 n \mu_c} \tag{1}$$

where N is the density of free carriers, n is the refractive index, $\in_0$ is the permittivity of free space, c is the speed of light, m_c^* is the effective mass of the carrier and μ_c is the conductivity mobility. The Drude model has been proven to accurately predict free carrier absorption in the mid- to far-IR ($\lambda > 2$ μm) [7, 8], where the smaller momentum changes decrease the dependence on scattering probabilities. For near IR wavelengths (1 μm $< \lambda <$ 2 μm) the classical Drude–Zener theory breaks down leading to inaccurate prediction of the absorption spectrum [9]. Koskowich *et al* [10] have obtained good fits to the experimental absorption spectrum in this range using a generalized theory that accounts for non-parabolic band structure, the multiple valleys in the bands and introduction of an additional first-order interaction with a dispersionless phonon in addition to acoustic and optical phonon scattering. Regardless of these complications, the basic feature of the generalized theory is the linear dependence of the free-carrier absorption coefficient α on N (actually $\alpha(N) \propto \sqrt{N(N+1)} \simeq N$ [10]). In a photoexcited semiconductor, assuming trapping effects are negligible, the electrons and holes will recombine in pairs and the free carrier absorption will be the sum of the contributions from both electrons and holes, despite the fact that their photon capture cross sections may differ [11]. In addition to the IR absorption by injected carriers, there will be a residual IR absorption background level due to the equilibrium carrier density and phonon scattering [10]. Furthermore, spectral features are superposed on the photon–lattice–phonon interactions due to the presence of band-gap defect and impurity states [12–14] which raise the possibility of band-to-defect or band-to-impurity state recombination transitions, the latter being a function of doping density [15].

The reverse process of free-carrier absorption (free-carrier radiative emission) also occurs naturally as a consequence of Kirchhoff's law of detailed balance [16, 17]. In indirect semiconductors like Si, at room temperature, it is manifested as very weak infrared recombination emission, a room-temperature photoluminescence (PL), induced by low-quantum-yield band-to-defect or impurity-state radiative recombination [18–20]. Conventional room-temperature PL in Si has rarely been reported and it invariably involves band-to-band bipolar recombination via photo-excited electron and hole excess densities in the high-injection regime ($>10^{16}$ cm^{-3}). Room-temperature PL is generally a nonlinear two-body process of electron–hole band-to-band recombination at high photo-excitation densities. It is fast ($\sim$2.9 μs decay time [19]) and thus requires considerably high frequencies to be detected under harmonic optical excitation (100 kHz–10 MHz). King and Hall have performed spectroscopic studies of near band-edge PL emissions from silicon [18] at 30 K, 130 K and 300 K in the spectral region between 1000 nm and 1700 nm. They used a liquid-nitrogen-cooled InAs detector and reported two broadened peaks at 300 K: one peak approximately centred at 1120 nm very near the band-edge, due to band-to-band electron–hole recombination, and a more prominent peak centred at about 1700 nm which was identified as the P line [20] and was associated with radiative emissions from recombination at an unidentified defect complex in which oxygen plays a central role. They also measured the external quantum efficiency of the process(es) involved in the PL emission and found it to be about 2.5×10^{-5} at 300 K.

Photo-carrier radiometry (PCR) [17] is a form of quantitative modulated photoluminescence and consists of radiative emissions in a semiconductor. In silicon, owing to the very low quantum yield of the process [20], at room [17] or higher [21] temperatures, PCR consists of optical excitation responses of the semiconductor characteristic of band-to-impurity or defect recombination, although quadratic-range band-edge recombination-induced signals involving electron–hole pairs have been observed as expected from two-carrier recombination kinetics [19, 22]. Frequency domain PCR has become possible by virtue of lock-in detection, the superior signal-to-noise ratio (SNR) and the non-thermal noise nature of the infrared InGaAs detectors typically used in its experimental implementation. This technique has been introduced to study electronic kinetic and recombination phenomena and has yielded signal interpretations in terms of electronic carrier diffusive transport under harmonic excitation, the so-called carrier diffusion density wave (CDW) [23]. PCR uses a narrow spectral window to detect near-band-gap infrared CDW emissions. This non-equilibrium radiative emission is a manifestation of detailed balance. PCR [17] is distinct from the aforementioned photoluminescent processes [19] as operation in the sub-quadratic optical excitation regime requires much lower frequencies than electron–hole band-to-band recombination and considerably higher signal dynamic range of the detection apparatus. Guidotti

et al [22] reported their inability to monitor very weak PL in the low-modulation-frequency (∼kHz) linear regime (where PCR operates) and have confined their studies to the quadratic band-to-band recombination regime (>10 kHz, mostly >1 MHz for highest strength signals). As a result, PCR appears to be significantly more sensitive to band-to-impurity or band-to-defect recombination than earlier modulated room-temperature PL techniques [19, 22] and can monitor subtler nonlinearities in the power of the optical excitation source, such as near-surface band-bending space-charge-layer processes [24] free of domination by quadratic recombination. The sub-quadratic character of PCR to excitation intensity is of crucial importance to the cross-modulation phenomena described in this work which carry their own nonlinear signatures.

Recently, a new version of photocarrier radiometry using a secondary subband-gap dc light source was introduced and was applied to deep sub-surface electronic defect imaging in Si wafers [25]. It was found that the use of a dc light source superposed on the modulated laser beam drastically enhances the potential of the technique to resolve low-level deliberate damage otherwise virtually indistinguishable by conventional PCR, photothermal techniques [26], or conventional transmission optical spectroscopy. Qualitatively, this contrast amplification can be understood within the framework of free-carrier distribution depth profile modifications by enhanced non-radiative recombination at localized or extended defects either at the semiconductor surface or inside the bulk. A qualitative understanding of how the addition of a subband-gap laser beam (an IR dc light source) with spectral content within the PCR detector bandwidth amplifies signal contrast has emerged [25]. The almost transparent semiconductor acts as a lossy multipass medium for the subband-gap radiation, the latter being multiply inter-reflected inside the sample and controlled by the effective reflectivity of the combined back surface and IR-reflecting backing support. The loss factor is controlled by the superband-gap laser source-induced infrared coefficient depth profile, in the detailed balance sense [17]. This, in turn, cross-modulates the intensity of the dc subband-gap radiation which is spatially coincident with the modulated absorption/emission depth profile and is superposed on the direct back-propagated emission signal from recombining carriers. The dc light is synchronously detected by the PCR detector. To first order, recombination features localized within the interaction volume of the two beams contribute to the CDW infrared absorption/emission coefficient distribution profile (and its spectral integral at the detector), resulting in contrast enhancement from ionic impurities and electronic trap densities by virtue of the cumulative effect of multipass attenuation of the IR radiation field inside the semiconductor crystal. The finite absorption of the photo-excited free-carrier density wave raised by the superband-gap beam amounts to an interaction which results in the latter beam cross-modulating the subband-gap beam in a manner formally equivalent to an optoelectronic chopper in the bulk of the semiconductor. The presence of the subband-gap beam enhances the dependence of the PCR signal on the details of the local free-carrier profiles and thus acts as an amplifier of the *local* absorption/emission characteristics as controlled by the CDW diffusion length [21]. Additional second-order optical features due to the interaction of the two beams, such as the potential decrease of the residual subband-gap absorption coefficient due to changes in the carrier capture cross-section, leading to depletion of occupied band-gap states by virtue of the presence of radiative recombination photons, may further enhance the effects of optical and/or electronic inhomogeneities, thus contributing to sub-surface imaging contrast.

In this paper, a quantitative basis of the dual-beam physical processes involved in PCR is developed and detailed experimental validations of the theory are presented, including imaging of Fe-contaminated and H^+ implanted p-type Si wafers. A few authors have previously used a combination of modulated superband-gap laser beam and a superposed subband-gap probe beam in transmission [11, 27, 28]. However, they have only been concerned with the effects of measuring the free-carrier transport parameters through the absorption of the transmitted subband-gap beam itself, while ignoring or being unable to measure the superposition interaction effects of the superband-gap beam, including PL. Characteristically, Mroczkowski *et al* [11] reported that no PL was observed due to the modulated pump beam. It is clear that the defect/impurity contrast amplification scheme which originates in the interaction of both beams through the cross-modulation mechanism of the subband-gap beam by the modulated superband-gap source, is germane to the nature of PCR as a radiative recombination emission technique sensitive to band-gap defect and/or impurity states. This underscores the PCR potential for ultra-sensitive subsurface contamination and defect imaging applications some of which are reported in this work.

2. Dual-beam PCR cross-modulation theory

2.1. Cross-modulation of a subband-gap laser beam

Assuming a superband-gap modulated optical source raising a spatial distribution of free photoexcited carriers in a semiconductor, two processes are likely to occur upon release of recombination emission photons which constitute the conventional PCR signal: (1) re-absorption of radiative recombination emissions at particular energy levels such that $|E_G - E_d| = \hbar\omega_0 \pm \hbar\Omega_{Ph}$, where E_G is the band-gap energy, E_d is the energetic level of the trap state in which the optically released carrier resides, ω_0 is the optical angular frequency of the exciting recombination photon, and Ω_{Ph} is the vibration frequency of the phonon which is absorbed or emitted during the optical transition in indirect-gap semiconductors like Si. (2) If an IR subband-gap laser beam is also present, further selective absorption of the IR radiation field occurs due to any band-defect or band-impurity optical transitions compatible with the energetic configuration of the material. During the former process (1), in a semiconductor of thickness L, the IR absorptance (defined as the absorption coefficient multiplied by the total absorption length for a single pass, L) can be written as

$$A_{(q,p)}(\lambda_{PCR};\omega) = C(E)\int_{pL}^{qL} \Delta N(z,\omega)\,\mathrm{d}z. \qquad (2)$$

Here, the integers $p, q\ (\geqslant 0)$ signify passes across the thickness of the semiconductor: $p = 0$, $q = 1$ represents the first pass,

$p = 1$, $q = 2$ represents the contribution of the second pass after one reflection at the back surface, etc, $\Delta N(z, \omega)$ is the excess carrier free density and $C(E)$ is the capture cross section for the carriers contributing to the PCR signal at the mean energy $E = hc/\lambda_{\mathrm{PCR}}$, where λ_{PCR} is the mean IR emission wavelength.

It should be emphasized that the values $p > 1$ and $q > 0$ in the limits of the integral above represent no different absorption coefficients from that obtained with the values $q = 1$ and $p = 0$, but, rather, the higher-pass contributions to the recombination-generated IR photons to the overall absorption inside the body of the semiconductor. The latter process (2) arises when the two beams are coincident, because the IR absorption coefficient corresponding to the wavelength of the subband-gap beam can be further modified (decreased) when the superband-gap beam is turned on. This is a secondary effect and in the opposite direction of the (usually dominant) increase of the IR absorption coefficient when a free-carrier density is optically generated by the superband-gap laser beam as described by equation (2). Incidence of the modulated superband-gap laser modifies the population of defect/impurity energy states within a carrier diffusion length because radiatively emitted recombination photons induce some empty band-gap states through absorption-induced transitions to the respective conduction or valence band, thus eliminating some subsequent absorption events upon passage of the subband-gap IR beam. The density of thus created empty band-gap states can be significant in the case of PCR (and other optical techniques) where the optical injection is relatively high in the 10^{17}–10^{19} cm^{-3} range [29]. Respective subband-gap absorption events would be present, if the superband-gap beam were turned off. Therefore, the modified probability for IR absorption can be described as a decreased absorptance with an effective free-carrier capture cross-section decreased proportionally to the peak intensity, $I_{\mathrm{ac},0}$, of the incident superband-gap beam:

$$A_{M(q,p)}(\lambda_{\mathrm{IR}}; \omega) = [C(E) - BI_{\mathrm{ac},0}] \int_{pL}^{qL} \Delta N(z, \omega)\, \mathrm{d}z. \quad (3)$$

Note that use of the subband-gap beam wavelength λ_{IR} in equation (3) denotes absorption phenomena solely concerning the subband-gap beam, whereas the use of λ_{PCR} in equation (2) is indicative of PCR emissions, usually of a broader spectral content than the monochromatic subband-gap laser beam, regardless of the presence of the latter. In principle, the two contributions to the overall PCR signal at the detector can be spectrally separated out with suitable band-pass filters. In practice, both types of infrared photons impinge on, and are detected by, the same broadband PCR detector. In equation (3), B is an optoelectronic constant of the semiconductor describing the change in free-carrier capture cross-section upon the presence of the recombination photon inducing superband-gap beam. In the limit $I_{\mathrm{ac},0} = 0$, the two coefficients $A_{(q,p)}(\lambda_{\mathrm{PCR}}; \omega)$ and $A_{M(q,p)}(\lambda_{\mathrm{IR}}; \omega)$ coincide, as expected. In this limit ΔN represents the residual free-carrier density. Under harmonic modulation of the superband-gap laser beam with angular frequency ω, the time-dependent incident intensity $I_{\mathrm{ac}}(t)$ is given by

$$I_{\mathrm{ac}}(t) = \tfrac{1}{2} I_{\mathrm{ac},0}(1 + \mathrm{e}^{\mathrm{i}\omega t}) \rightarrow I_{\mathrm{ac},0}\, \mathrm{e}^{\mathrm{i}\omega t}. \quad (4)$$

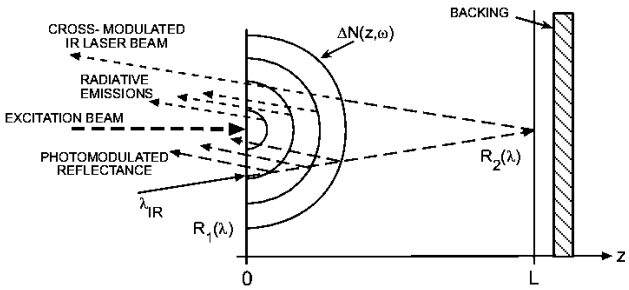

Figure 1. Schematic cross-section of a semiconductor supported by a backing under optical excitation with a modulated superband-gap laser beam superposed on an unmodulated subband-gap laser beam of wavelength λ_{IR}. Iso-density contours of the free-carrier density $\Delta N(z, \omega)$ are shown as the source of modulated reflectance. R_1 and R_2 are the reflectances of the front and back surfaces, respectively.

The second form of the equation is a simplification of the modulation factor. Figure 1 shows a schematic cross-section of a semiconductor of thickness L and the optical paths of an incident superband-gap excitation laser beam modulated at angular frequency ω, another incident unmodulated subband-gap laser beam, as well as the PCR emissions in the back-propagation configuration. To complete the physical picture, contributions to the photomodulated reflectance of the subband-gap beam are shown, the result of the modulated carrier density gradient generated by the superband-gap beam. Assuming that the photomodulated reflectance is dominated by the Drude component [30], one may write

$$R_1(\omega) = R_{10} + \Delta R_1\, \mathrm{e}^{\mathrm{i}\omega t} \quad (5)$$

where R_{10} is the dc optical reflectance and ΔR_1 is the modulated component of the reflectance in the presence of the excess carrier density-wave $\Delta N(z, \omega)$. The incident laser beams in figure 1 are angularly resolved for clarity, but in our experiments they were directed normal to the surface. It is assumed that the mean modulated infrared absorption coefficient within the bandwidth of the PCR detector (InGaAs Thorlabs model PDA400 with a spectral bandwidth of 800–1750 nm) is $\alpha(z, \omega)$. This depth-dependent coefficient is given by equation (1) with $N \rightarrow \Delta N(z, \omega)\, \mathrm{e}^{\mathrm{i}\omega t}$ ('photomodulated reflectance') to denote excess free-carrier density. At the surface $z = 0$ the contribution from the back-propagating subband-gap beam undergoing infinite inter-reflections in the presence of $\alpha(z, \omega)$ is given by adding up all the back-propagating infrared emission 'light rays':

$$I_{\mathrm{dc}}(0) \equiv I_{\mathrm{R}} = I_{\mathrm{dc},0} \left[R_1 + (1 - R_1)^2 R_2 \sum_{n=0}^{\infty} (R_1 R_2)^n \times \exp\left(- \int_0^{2(n+1)L} \alpha(z, \omega)\, \mathrm{d}z \right) \right]. \quad (6)$$

It will be noted that both R_1 and $\alpha(z)$ are functions of modulation frequency by virtue of their dependence on $\Delta N(z, \omega)\, \mathrm{e}^{\mathrm{i}\omega t}$. Equation (6), in the limiting case $\alpha(z) = \text{const.} = \alpha_0$, yields the well-known reflectance expression [31]

$$I_{\mathrm{dc}}(0) = I_{\mathrm{dc},0} \left[R_1 + \frac{(1 - R_1)^2 R_2\, \mathrm{e}^{-2\alpha_0 L}}{1 - R_1 R_2\, \mathrm{e}^{-2\alpha_0 L}} \right]. \quad (7)$$

The infinite series in equation (6) cannot be summed up compactly as a geometric progression, because

$$\exp\left(-\int_0^{2(n+1)L}\alpha(z,\omega)\,\mathrm{d}z\right) \neq \exp\left(-(n+1)\int_0^{2L}\alpha(z,\omega)\,\mathrm{d}z\right) \tag{8}$$

for all functional depth dependences of $\alpha(z)$ other than a constant value.

Now using the identity

$$\exp\left[-\mathrm{e}^{\mathrm{i}\omega t}\int_0^{2(n+1)L}\alpha(z,\omega)\,\mathrm{d}z\right] = 1-\mathrm{e}^{\mathrm{i}\omega t}\int_0^{2(n+1)L}\alpha(z,\omega)\,\mathrm{d}z+\sum_{n=2}^{\infty}(-1)^n O(\mathrm{e}^{\mathrm{i}n\omega t}) \tag{9}$$

we write the IR absorption coefficient at the mean detection wavelength λ_{PCR} of the PCR signal as a sum of the background (residual) absorption coefficient at equilibrium and a photo-carrier density dependent component:

$$\alpha(z,\omega)=\alpha_0+\alpha(z,\omega)\,\mathrm{e}^{\mathrm{i}\omega t}. \tag{10}$$

Substituting equations (5) and (10) into equation (6), carrying out the spectral (Fourier) decomposition (9), collecting terms up to $O(\mathrm{e}^{\mathrm{i}\omega t})$ and retaining only terms of this order in view of the experimental requirement for lock-in amplifier signal detection at the fundamental frequency, ω, we find for the reflected fraction of the incident subband-gap radiation intensity

$$F(\lambda_{\mathrm{IR}};\omega)\equiv\frac{I_{\mathrm{R}}}{I_{\mathrm{dc},0}}=\Delta R_1(\omega)\left(1-\frac{(1-R_{10})R_2\,\mathrm{e}^{-2\alpha_0 L}}{1-R_{10}R_2\,\mathrm{e}^{-2\alpha_0 L}}\times\left[2-\frac{(1-R_{10})R_2\,\mathrm{e}^{-2\alpha_0 L}}{1-R_{10}R_2\,\mathrm{e}^{-2\alpha_0 L}}\right]\right)-(1-R_{10})^2R_2\times\sum_{n=0}^{\infty}(R_{10}R_2)^n A_{M[2(n+1),0]}(\lambda_{\mathrm{IR}};\omega)\,\mathrm{e}^{-2(n+1)\alpha_0 L}. \tag{11}$$

Here the multiplicative modulation factor $\mathrm{e}^{\mathrm{i}\omega t}$ is implied on the rhs. Equation (11) identifies the contribution of the subband-gap beam intensity at the fundamental modulation frequency ω through photomodulation (positive term) and cross-modulation (negative term) by virtue of the presence of the superposed superband-gap beam, a highly nonlinear process which in principle involves all higher harmonic orders of ω.

2.2. PCR emission intensity

In the semiconductor cross-sectional picture of figure 2 it can be shown that the back-propagating contribution of radiative emissive power $\mathrm{d}P_{\mathrm{R}}$ from a slice $\mathrm{d}z$ at depth z, when infinite inter-reflections from both semiconductor surfaces are included, can be written as [17]

$$\mathrm{d}P_{\mathrm{R}}(z:\omega)=\eta_{\mathrm{R}}W_{\mathrm{R}}\left[\sum_{n=0}^{\infty}R_1^nR_2^n\alpha(2nL+z;\omega)\times\exp\left(-\int_0^{2nL+z}\alpha(2nL+z';\omega)\,\mathrm{d}z'\right)+(1-R_1)R_2\sum_{n=0}^{\infty}R_1^nR_2^n\alpha[2(n+1)L-z]\times\exp\left(-\int_0^{2(n+1)L-z}\alpha[2(n+1)L-z']\,\mathrm{d}z'\right)\right]\mathrm{d}z \tag{12}$$

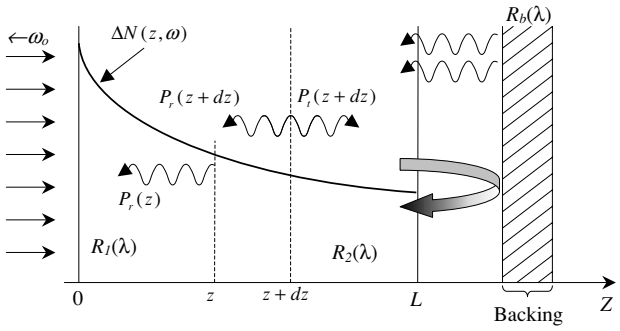

Figure 2. Cross-sectional view of contributions to front-surface radiative emissions of IR photons from a semiconductor strip of thickness $\mathrm{d}z$ at depth z. The carrier-wave depth profile $\Delta N(z,\omega)$ results in a depth dependent IR absorption/emission coefficient due to free-carrier absorption of the infrared recombination photon field. $P_j(z)$ is the probability that a photon emitted by means of radiative recombination emerges in the backwards (r) or forward (t) direction.

where η_{R} is the quantum yield for an optical transition from the valence to the conduction band and W_{R} is the effective optical emission power emitted by means of radiative recombination of the photo-excited carrier. This expression can be simplified upon noting that $\alpha(2L+z)=\alpha(4L+z)=\cdots=\alpha(2nL+z)=\alpha(z)$; and $\alpha(2L-z)=\alpha(4L-z)=\cdots=\alpha[2(n+1)L-z]=\alpha(z)$. The total back-propagated radiative photo-carrier radiometric intensity from the entire depth of the semiconductor, emitted through a cross-sectional area A of surface, is found to be

$$I_{\mathrm{PCR}}(\omega)=\frac{1}{A}\int_0^L\mathrm{d}P_{\mathrm{R}}(z;\omega)\,\mathrm{d}z=I_{\mathrm{eR}}\sum_{n=0}^{\infty}(R_1R_2)^n\times\left[J_n(\omega)+(1-R_1)R_2J_{n+\frac{1}{2}}(\omega)\right] \tag{13}$$

where I_{eR} is the effective radiative emission intensity and

$$J_n(\omega)\equiv\left[1-\exp\left(-\int_{2nL}^{(2n+1)L}\alpha(z';\omega)\,\mathrm{d}z'\right)\right]\times\exp\left(-\int_0^{2nL}\alpha(z';\omega)\,\mathrm{d}z'\right),\qquad n\geqslant 0. \tag{14}$$

In the limit of $\alpha(z)=\text{const.}=\alpha_0$, equation (13) readily yields

$$I_{\mathrm{PCR}}(\alpha_0;\omega)=I_{\mathrm{eR}}\left[\frac{1+(1-R_1)R_2\,\mathrm{e}^{-\alpha_0 L}}{1-R_1R_2\,\mathrm{e}^{-2\alpha_0 L}}\right](1-\mathrm{e}^{-\alpha_0 L}). \tag{15}$$

The reflectances R_1 and R_2 are associated with the mean infrared recombination radiation emission, but they can be taken to be equal to the respective quantities corresponding to the unmodulated IR laser beam by virtue of the vicinity of the wavelengths of the two radiation sources, at least within the spectral bandwidth of the detector. Therefore, $R_1=R_{10}$. Finally, when equation (11) is taken into account, one obtains for the complete radiation intensity impinging on the PCR detector:

$$I_{\mathrm{T}}(\omega)=I_{\mathrm{R}}(\lambda_{\mathrm{IR}};\omega)+I_{\mathrm{PCR}}(\lambda_{\mathrm{PCR}};\omega)=I_{\mathrm{eR}}\sum_{n=0}^{\infty}(R_{10}R_2)^n\{[A_{(2n+1,2n)}(\lambda_{\mathrm{PCR}};\omega)\,\mathrm{e}^{-\alpha_0 L}$$

$$- A_{(2n,0)}(\lambda_{PCR};\omega)(1-e^{-\alpha_0 L})]\,e^{-2n\alpha_0 L} + (1-R_{10})R_2$$
$$\times [[A_{[2(n+1),2n+1]}(\lambda_{PCR};\omega)\,e^{-\alpha_0 L} - A_{(2n+1,0)}(\lambda_{PCR};\omega)$$
$$\times(1-e^{-\alpha_0 L})]\,e^{-(2n+1)\alpha_0 L}]\} - I_{dc,0}(1-R_{10})^2 R_2$$
$$\times \sum_{n=0}^{\infty}(R_{10}R_2)^n A_{M[2(n+1),0]}(\lambda_{IR};\omega)\,e^{-2(n+1)\alpha_0 L}$$
$$+ I_{dc,0}\Delta R_1(\omega)\left(1 - \frac{(1-R_{10})R_2\,e^{-2\alpha_0 L}}{1-R_{10}R_2\,e^{-2\alpha_0 L}}\right.$$
$$\left.\times\left[2 - \frac{(1-R_{10})R_2\,e^{-2\alpha_0 L}}{1-R_{10}R_2\,e^{-2\alpha_0 L}}\right]\right). \qquad (16)$$

Significant simplification of the foregoing expression can be deduced in the case of conventional silicon wafers which have a polished front surface and a matte (microscopically rough) back surface. Assuming that the photomodulated reflectance is dominated by the Drude component, one may approximate

$$\Delta R_1 \approx \frac{\partial R}{\partial N}\Delta N_{\text{eff}} \approx \frac{\partial R}{\partial N}\Delta N \qquad (z=0,\omega) \qquad (17a)$$

where [32]

$$\frac{\partial R}{\partial N} \approx -\frac{\lambda^2 e^2}{2\pi^2\varepsilon_0 m^* c^2}\frac{n-1}{n(n+1)^3} = -6.275\times 10^{-29}\ \text{m}^3 \qquad (17b)$$

The values used to calculate this number are: $\lambda = 1550$ nm, $e = 1.6\times10^{-19}$ C, $m^* = 0.156m_o$, $m_o = 9.1\times10^{-31}$ kg, $c = 2.998\times10^8$ m s^{-1}, n ($\lambda = 1550$ nm) $= 3.478$, $\varepsilon_0 = 8.854\times10^{-12}$ C^2 N^{-1} m^{-2}. The value of $\partial R/\partial N$ is of the same order found experimentally and theoretically by Wagner [32] for $\lambda = 632$ nm. Simulations showed that this contribution is much less than the absorption of the IR laser beam and has a negligible effect on the overall subband-gap signal. Therefore, it can be safely ignored in equation (16) in favour of cross-modulation in applications to semiconductor silicon. Furthermore, the contributions from multiple passes amount to much lower back-propagated intensity from the photoreflectance mechanism than the first reflection due to the matte (scattering) nature of the back surface. This leaves only the fundamental component $n = 0$ in expression (16) so that the various integrals become

$$A_{[2(n+1),2n]}(\lambda_{PCR};\omega) = A_{(2,0)}(\lambda_{PCR};\omega)$$
$$A_{(2n,0)}(\lambda_{PCR};\omega) = A_{(0,0)}(\lambda_{PCR};\omega) = 0$$
$$A_{[2(n+1),2n+1]}(\lambda_{PCR};\omega) = A_{(2,1)}(\lambda_{PCR};\omega)$$
$$A_{[2n+1,0]}(\lambda_{PCR};\omega) = A_{(1,0)}(\lambda_{PCR};\omega)$$
$$A_{M[2(n+1),0]}(\lambda_{IR};\omega) = A_{M(2,0)}(\lambda_{IR};\omega).$$

The experimentally relevant expression to silicon cross-modulation PCR, equation (16), becomes

$$I_T(\omega) = I_{eR}C(E)\left\{[e^{-\alpha_0 L} - (1-R_{10})R_2(1-e^{-\alpha_0 L})]\right.$$
$$\times\int_0^L \Delta N(z,\omega)\,dz + (1-R_{10})R_2\,e^{-\alpha_0 L}$$
$$\left.\times\int_L^{2L}\Delta N(z,\omega)\,dz\right\} - I_{dc}(1-R_{10})^2R_2\,e^{-2\alpha_0 L}$$
$$\times[C(E) - AI_{ac,0}]\int_0^{2L}\Delta N(z,\omega)\,dz. \qquad (18)$$

It has been assumed that the dimensions of the excitation source are such that the carrier density wave is one-dimensional so that the carrier density in the above equations can be expressed as [23]

$$\Delta N(z,\omega) = \frac{\eta_Q I_{ac,0}\alpha}{2\hbar\omega_o D^*(\alpha^2-\sigma_e^2)}\left\{\left(\frac{\Gamma_2\gamma_1 - \gamma_2\Gamma_1\,e^{-(\sigma_e+\alpha)L}}{\Gamma_2 - \Gamma_1\,e^{-2\sigma_e L}}\right)\right.$$
$$\left.\times\,e^{-\sigma_e z} + \left(\frac{\gamma_1 - \gamma_2\,e^{-(\alpha-\sigma_e)L}}{\Gamma_2 - \Gamma_1\,e^{-2\sigma_e L}}\right)e^{-\sigma_e(2L-z)} - e^{-\alpha z}\right\} \qquad (19)$$

where

$$\Gamma_1 \equiv \frac{D^*\sigma_e(\omega) - S_1}{D^*\sigma_e(\omega) + S_1} \qquad (20a)$$
$$\Gamma_2 \equiv \frac{D^*\sigma_e(\omega) + S_2}{D^*\sigma_e(\omega) - S_2} \qquad (20b)$$
$$\gamma_1 \equiv \frac{D^*\alpha + S_1}{D^*\sigma_e + S_1} \qquad (20c)$$
$$\gamma_2 \equiv \frac{D^*\alpha - S_2}{D^*\sigma_e - S_2} \qquad (20d)$$

η_Q is the optical to electronic quantum efficiency, I_0 is the intensity of the superband-gap excitation laser beam, α is the absorption coefficient at the excitation wavelength, D^* is the ambipolar diffusion coefficient and σ_e is the carrier wave number:

$$\sigma_e(\omega) = \sqrt{\frac{1+i\omega\tau}{D^*\tau}}. \qquad (21)$$

Here τ is the recombination lifetime, a free-carrier decay rate which depends on both radiative and non-radiative recombination events, as well as on higher-order (nonlinear) effects, such as Auger recombination [33].

3. Simulations of the cross-modulation PCR theory

The integrals of equation (18) were evaluated analytically and the dependence of the total two-beam PCR signal is plotted below as a function of various parameters. The secondary dc IR light traverses the sample and experiences multiple reflections at the front and back surface. The dc source is attenuated according to the IR absorption profile in the sample which is directly correlated to the carrier density profile. The portion of the IR laser beam exiting the front surface of the sample is superposed over the direct ac emissions from the recombining carrier wave and focused onto the detector. The direct radiative emissions will be in phase with the excited carrier density while the cross-modulated IR laser beam will have a maximum intensity when the carrier density is lowest and is therefore out of phase with the excitation source. This is indicated by the minus sign of the last term in equation (18). Thus the two contributions to the PCR signal will be 180° out of phase with respect to one another. Since the overall signal is the vectorial sum of the two complex contributions, the introduction of the IR beam will initially act to decrease the signal until the magnitude of this secondary source approaches that of the direct radiative emissions. As the intensity of the IR laser increases further the total signal reaches a minimum and proceeds to increase as the cross-modulated IR laser component becomes increasingly dominant. The

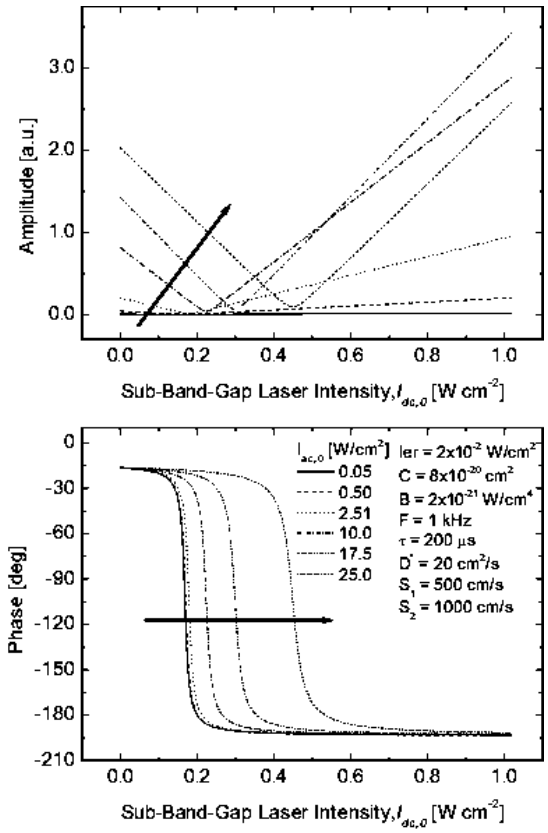

Figure 3. Simulation of cross-modulation PCR theory for various values of ac super-band-gap laser intensity, $I_{ac,0}$. Arrows indicate trends for increasing values of $I_{ac,0}$.

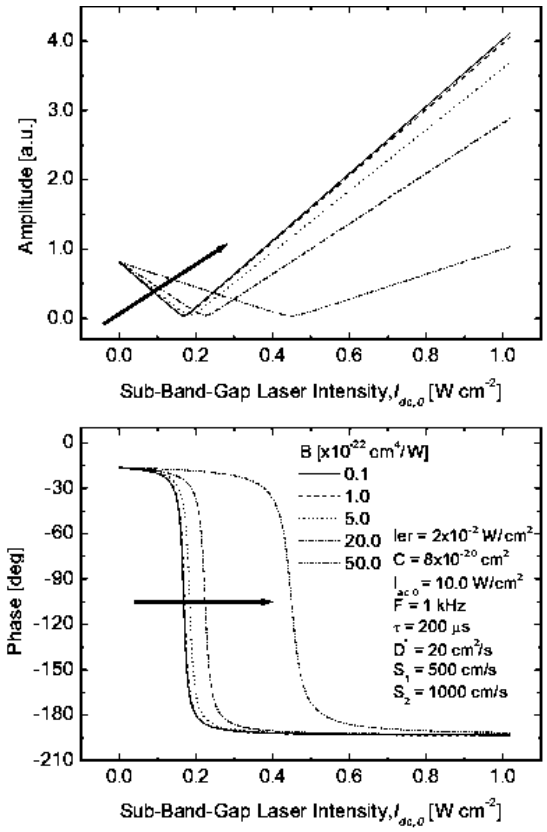

Figure 4. Simulation of cross-modulation PCR theory for various values of B. Arrows indicate trends for increasing values of B.

power at which the secondary laser begins to dominate the radiative emissions is also designated by a rapid phase change of 180° since the two contributing mechanisms are out of phase. The resulting amplitude and phase as a function of dc IR laser intensity $I_{dc,0}$ is shown for various ac superband-gap laser intensities in figure 3. For larger ac superband-gap laser intensities the increasing number of photogenerated carriers results in a greater number of radiative emissions and hence a larger PCR signal at $I_{dc,0}$. The number of IR laser photons required to induce a transition of the dominant signal generation mechanism increases proportionally to the radiative emissions, causing the PCR amplitude minimum and phase shift to move to higher $I_{dc,0}$ intensities as the intensity of the superband-gap excitation source increases.

The reabsorption of recombination-induced radiative emissions modifies the occupation of defect/impurity states and thus the free-carrier capture cross-section. The influence of this perturbation on the absorption of the IR laser beam is represented in the mathematical model by the constant B, and the effect on the total signal is presented in figure 4. A larger value of B represents more efficient reabsorption of the radiative emissions resulting in a corresponding lower probability of absorption for an IR laser photon, and thus a greater sensitivity of the absorptance of the IR laser to the carrier injection level. For a fixed super-band-gap laser intensity, as B increases, the absorptance of the IR laser beam decreases and a greater intensity of the dc laser beam is required to achieve a cross-modulated IR beam amplitude of sufficient magnitude to dominate the radiative PCR emissions and induce the corresponding 180° phase shift in the combined PCR signal.

The influence of carrier recombination lifetime on the dc IR laser power scans is shown in figure 5. Higher lifetimes result in steeper amplitude slopes because the longer presence of carriers enhances the probability of an IR photon absorption event, increasing the depth of modulation of the IR laser beam everywhere in the photo-excited volume and, in particular, in the interaction region between the two beams. Thus, the amplitude of the modulated portion of the IR laser beam exiting the sample also increases. The direct influence of the lifetime on the radiative emissions is stronger than the indirect effect on the IR absorption processes, resulting in a shift of the cross-over point to higher dc laser powers. There is an increase in the phase lag as the lifetime becomes longer than the modulation period resulting in a temporal separation between the generation source and the carrier density that is manifested as a phase lag and a rounding of the onset and saturation of the 180° phase transition in the frequency domain. The trends of figure 5 are valid for all modulation frequencies but as the frequency increases the sensitivity to lifetime decreases and eventually saturates. This decreasing sensitivity to lifetime at high frequencies is due to the fact that at frequencies such that $\omega\tau \gg 1$ the ac carrier diffusion length becomes independent of lifetime:

$$L_{ac} = \sqrt{\frac{D^*\tau}{1+i\omega\tau}} \xrightarrow{\omega\gg 1} \sqrt{\frac{D^*}{i\omega}}.$$

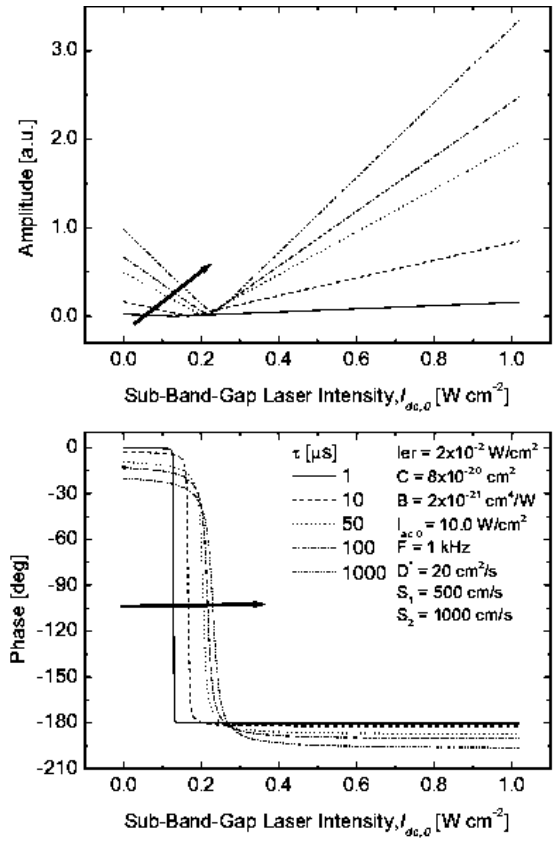

Figure 5. Simulation of cross-modulation PCR theory for various values of recombination lifetime. Arrows indicate trends for increasing values of τ. The slope of the amplitude 'v-curves' is a function of τ.

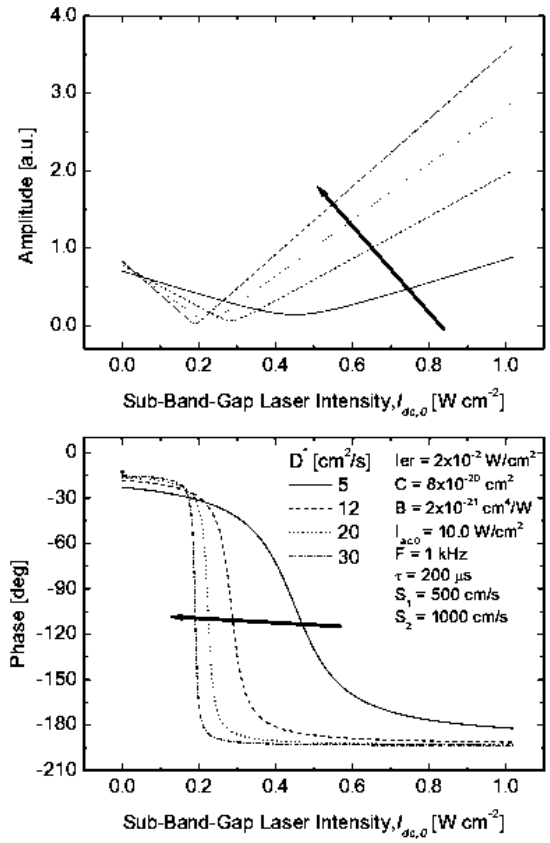

Figure 6. Simulation of cross-modulation PCR theory for various values of carrier ambipolar diffusion coefficient, spanning the range from n-type to p-type minority carrier recombination. Arrows indicate trends for increasing values of D^*.

The influence of the carrier ambipolar diffusion coefficient, D^*, on the IR laser power scans is shown in figure 6. Increasing the diffusion coefficient increases the slope of the amplitude 'v-curve' and shifts the cross-over point to lower IR laser powers. As the carrier density decreases due to a more rapidly diffusing (spreading) wave, it takes less IR power to overcome recombination induced emission effects. Simulations with the front surface recombination velocity equal to zero show similar results so the trends are not (at least entirely) a result of a diminishing influence of surface recombination with increasing diffusion away from the surface. A significant difference between the effects of the diffusion coefficient and the effects of the lifetime is the shift of the cross-over point to lower powers for increasing D^* and to higher powers for increasing lifetime. This suggests that the influence of D^* on the absorption of the IR laser is stronger than its influence on the radiative emissions and supports the hypothesis that the increasing slope is not only due to a decreasing sensitivity to front surface recombination but rather is dominated by the effect of the longer diffusion length on the absorptance of the IR beam. Similar trends were found throughout the frequency range of interest but the sensitivity to diffusivity is less at higher frequencies as the carrier diffusion length decreases and changes due to variations in D^* become relatively small.

The effects of the front surface recombination velocity on the signal are shown in figure 7. Enhanced surface recombination decreases the carrier density in the sample and thus lowers the amplitude of the PCR emissions as well as cross-modulation interaction with the IR laser beam. The lower absorptance decreases the modulation depth of the IR laser and thus the slope of the signal as a function of IR laser power. In contrast to the lifetime dependence, the variation of front surface recombination velocity has essentially no influence on the cross-over power for the frequency range of interest, except for a very slight influence at the high end of the frequency range. This suggests that until the diffusion length is very short and the carriers are confined to the very-near-surface region, the front surface recombination velocity acts essentially as a sink at $z = 0$ that decreases the overall carrier density but does not have a significant effect on the spatial (depth) profile, specifically, it does not alter the interaction volume with the subband-gap beam. Luke and Cheng [34] have shown that an increase in the front surface recombination velocity will result in a much more rapid decrease in the average number of carriers, but the evolution of the carrier density profile in an optically thick semiconductor similar to that considered here suggests that the carrier density profile will not vary significantly. In turn, the cross-modulated portion of the subband-gap beam decreases proportionately to the free-carrier density, independently of the absolute value of $I_{dc,0}$, thus leaving the minimum of the v-curve unchanged.

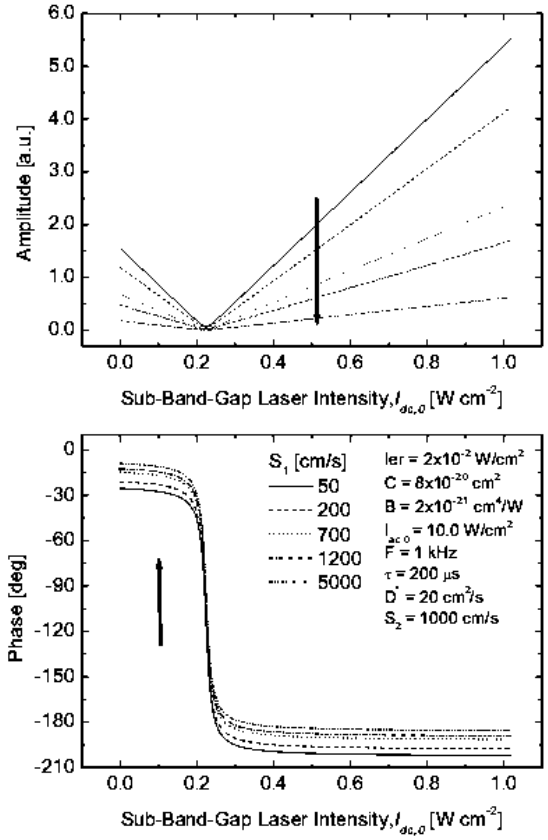

Figure 7. Simulation of cross-modulation PCR theory for various values of front surface recombination velocity. Arrows indicate trends for increasing values of S_1.

4. Experimental results—frequency and IR laser power scans

The experimental system for the two-laser-beam cross-modulation photocarrier radiometric system is shown in figure 8. A diode laser with an emission wavelength of 830 nm ('super-band-gap laser') is intensity modulated using a voltage supplied by a function generator and used as a carrier-wave generation source. A second laser ($\lambda = 1550$ nm, 3 mW laser diode) with a near-IR wavelength that lies within the bandwidth of the detector and has a photon energy slightly below the band gap of Si ('subband-gap laser') is introduced to the optical circuit of the PCR system through a cube beam splitter and is aligned collinear to the excitation laser beam. A linearly-variable neutral density filter is mounted on a motorized translation stage and placed in front of the IR laser to provide automated control of the subband-gap laser intensity. Both beams are focused using a gradium lens to a point coincident with the focal point of an off-axis paraboloidal mirror that collects a portion of any diffuse back-scattered photons. The system is designed such that the specular reflection of the two beams is not collected by the paraboloidal mirrors and thus is not focused onto the detector. The angle of incidence of the laser beams is $\sim 28^\circ$. The collected light is then focused onto an InGaAs detector with a switchable gain pre-amplifier built into the detector housing and a frequency response up to 10 MHz. The detector has a spectral bandwidth of 800–1750 nm with a peak response

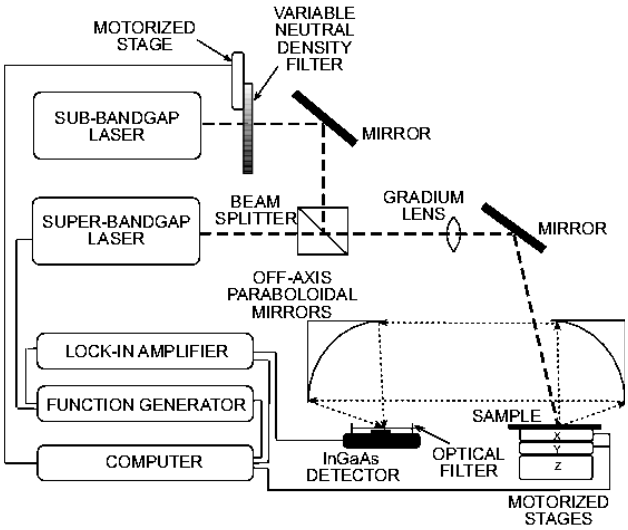

Figure 8. Schematic diagram of the two-beam cross-modulation PCR system.

at 1550 nm and an active element with a 1 mm diameter. A long-pass filter with a steep cut-on (5% at 1010 nm, 78% at 1060 nm) and a transmission range 1042–2198 nm is placed in front of the detector in order to ensure that any diffuse reflections of the excitation source do not contribute to the signal. The signal from the detector is demodulated by a lock-in amplifier. The sample holder is connected to a motorized *X–Y* stage assembly to allow for sample positioning and imaging and a third stage in the vertical direction is used to manually adjust the sample to the focal point of the collection optics. All instruments, data acquisition and sample positioning operations are controlled using a Matlab program.

Experimental frequency scans of a p-type Si wafer (640 μm thick, 20 Ω cm $\leqslant \rho \leqslant$ 40 Ω cm, 1000 Å thermally grown oxide) at various levels of absorption-modulated IR laser intensity relative to the radiative emission intensity (i.e. various IR laser powers) are shown in figures 9(*a*) and (*b*). For each frequency scan the super-band-gap excitation laser was modulated over a range of 10 Hz to 100 kHz while the sub-band-gap laser intensity remained fixed. Attempts to fit the experimental frequency scans to the theoretical model presented earlier were unsuccessful because the theory does not fully account for the dimensionality of the carrier transport and the relative size of the two laser beams. The theory assumes a one-dimensional geometry which requires a beam size that is large relative to the thickness of the sample and/or the detector size. Expansion of the excitation laser beam to a size suitable for the truly one-dimensional carrier transport did not provide sufficient intensities for acceptable signal-to-noise ratios in the absence of the subband-gap laser (i.e. conventional PCR). Fitting the three-dimensional results requires a much more detailed theory than that presented earlier that would have to account for the finite size and relative spatial intensity distribution of both laser beams, as well as lateral carrier diffusion and the corresponding change in the dimensionality of the problem, as the carrier diffusion length decreases with increasing modulation frequency. Simulated one-dimensional frequency scans at various levels of relative

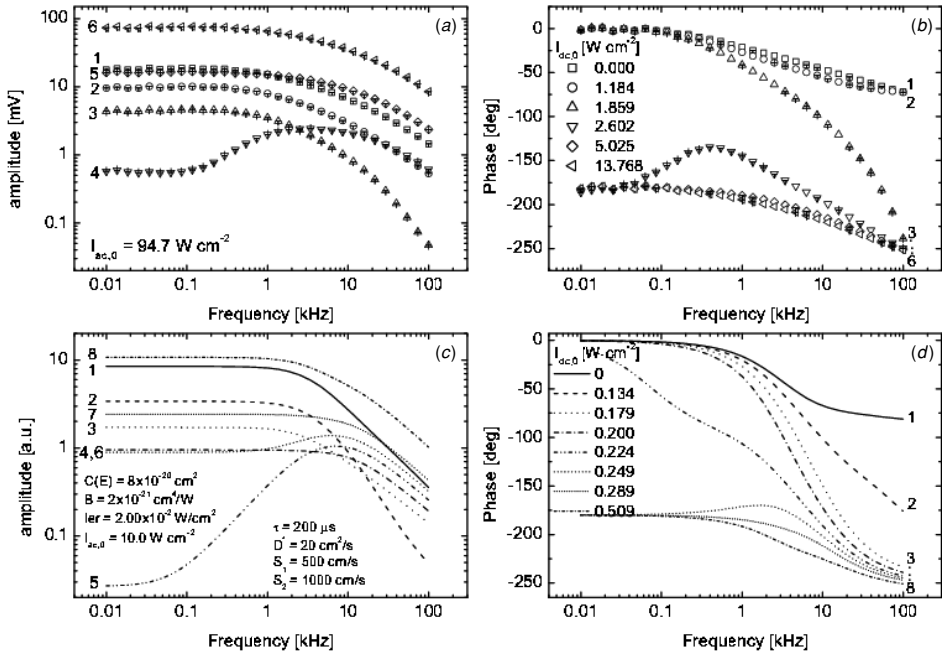

Figure 9. Experimental ((*a*) and (*b*)) and theoretical ((*c*) and (*d*)) modulation frequency scans at various relative levels of IR laser intensity.

IR laser intensity are shown in figures 9(*c*) and (*d*). The dependence of the frequency scan profile on IR laser intensity seen in the experimental curves is clearly evident in the simulations. Initially, as the IR laser power increases the amplitude decreases over the entire frequency range and the phase lag begins to increase only at high frequencies. Eventually, the high frequency phase will approach a minimum value that will be the phase at $I_{dc,0} = 0$ minus the approximately 180° phase shift resulting from the emerging dominance of the cross-modulated IR laser beam. In this range of IR laser powers the high-frequency signal is dominated by the IR laser beam and the low-frequency signal approaches the cross-over power but is still dominated by the recombination-induced radiative emissions. This results in a combined PCR signal amplitude that becomes larger at higher frequencies than at lower frequencies—a feature that is only possible in the presence of an external electrical field using conventional diffusion-wave-field characterization techniques. [23] As the IR laser power becomes large enough to dominate the recombination induced radiative emissions, the low frequency phase shifts 180° and the response begins to approach a similar profile to that when $I_{dc,0} = 0$ but shifted by 180°. The amplitude also approaches a profile similar to that at $I_{dc,0} = 0$ but the amplitude at each frequency will begin to scale linearly with further increases in IR laser power. Despite the inability to fit the frequency scans to the theory due to the dimensionality issues discussed earlier, the similarities between the experimental ((*a*) and (*b*)) and the theoretical ((*c*) and (*d*)) results presented in figure 9 demonstrate that the presented theory is useful for qualitative physical interpretation of the dual-beam frequency scans.

Although dimensionality issues prevented the exact fit of experimental frequency scans to theory, a methodology was developed to allow the theory to be fit to IR laser intensity scans performed at a fixed modulation frequency. Operating at a constant frequency results in a carrier distribution that does not change during the course of the scan and thus the dimensionality of the problem remains fixed. A dimensional transfer function that allows the one-dimensional cross-modulation PCR theory to be applied to the three-dimensional experiments was developed from the theoretical calculation of the one- and three-dimensional carrier-density-wave distributions using a set of transport parameters obtained from a multi-parameter fitting algorithm presented previously [17].

It is not useful to fit the IR laser power scans using a self-normalizing approach (meaning normalizing the amplitude of the first data point of the theoretical result to that of the experimental data) because this approach gives a multitude of possible solutions. The actual mathematical representation of the PCR signal must include an instrumental factor to account for the optical collection efficiency, the quantum efficiency of the detector and any electrical conditioning of the signal. Introduction of such a factor, γ, results in a final expression for the PCR signal:

$$S(\omega) = \gamma I_T(\omega)$$

where $I_T(\omega)$ is given in equation (18). Using the concept of a balance between emission and absorption, a value for the capture cross-section was assumed from the data of Schroder *et al* [35]:

$$C(E) \approx 10^{-18}\lambda^2$$

where λ is the wavelength in μm and $C(E)$ is in cm^2. Substitution of the infrared wavelengths of interest in this study was used to estimate the value at $C(E) \sim 2 \times 10^{-18}$ cm^2. Attempts were made to calculate the value of I_{eR}, which represents the effective intensity of IR photons emitted through recombination, using the internal quantum efficiency of 10^{-4}–10^{-6} published by King and Hall [18]. It was assumed that the off-axis paraboloidal mirror collects approximately

Table 1. Fitting results for IR laser intensity scans of figure 10.

Frequency (kHz)	0.1	1	10	100
$C(E) = 8.0 \times 10^{-20}$ cm^2 and $\gamma = 858$				
I_{eR} ($\times 10^{-2}$ W cm^{-2})	2.068	1.953	2.108	2.001
B ($\times 10^{-21}$ cm^4 W^{-1})	3.9726	4.1763	3.5869	4.0744
Error (%)	4.1723	10.346	3.9663	3.9996

1/12 of the total emitted radiation so that I_{eR} can be calculated as

$$I_{eR} \sim \frac{P_{ac}}{\pi w^2} \times \frac{10^{-5}}{12}.$$

Substituting the excitation laser power $P_{ac} = 20$ mW and the beam radius w of 252 μm the constant should have a value of $\sim 10^{-5}$ W cm^{-2}. While it was possible to fit a given set of experiments using values similar to those given above for $C(E)$ and I_{eR}, this resulted in a sensitivity to the super-band-gap laser intensity $I_{ac,0}$ that was much higher than found in experiments. The initial values of $C(E)$ and I_{eR} for fitting were thus chosen such that the theoretical sensitivity to $I_{ac,0}$ was consistent with the experimental results. These are unknown factors that multiply the integrals of the free carrier density to account for absorption in the sample. The exact values of these parameters cannot be studied in more detail without the ability to fit frequency scans. Regardless, proceeding with fitting the experiment to the theory shows the validity of the model in terms of the relationship between the two contributions to the total signal and the relative changes in these multiplying factors.

Since the theory best fits the high-frequency experiments, the instrumental factor γ was calculated using the 100 kHz data with $I_{eR} = 2.00 \times 10^{-2}$ W cm^{-2} and $C(E) = 8.0 \times 10^{-20}$ cm^2, which resulted in $\gamma = 858$. When fitting the curves for the remaining frequencies ($f = 0.1$, 1 and 10 kHz), knowledge of any two of the three variables remaining in equation (18) after setting $I_{dc,0} = 0$ (namely, $C(E)$, I_{eR} and γ) allows the third variable to be uniquely determined from the amplitude at $I_{dc,0} = 0$. The IR laser power scan was fitted using a least-squares method to determine the value of B. The remaining IR laser power scans were fitted by fixing $C(E)$ and γ to the initial values, adjusting I_{eR} to satisfy the $I_{dc,0} = 0$ amplitude for each curve, and leaving B as the sole free variable for fitting. The experimental scans and theoretical fits are shown in figure 10 and the extracted parameters are presented in table 1. B is frequency independent, as expected, with a measured value of $(3.95 \pm 0.26) \times 10^{-21}$ cm^4 W^{-1}. The fit at intermediate frequencies ($\sim$1 kHz) is of significantly lower quality due to the crudeness of the dimensionality transfer function approach and the fact that the sensitivity to dimensionality as discussed previously is greatest in this frequency range.

Two sets of experiments were designed to further investigate the validity of the proposed model. First, the unpolished surface of a high quality p-type Si wafer was lightly rubbed with optical paper to damage the surface. A frequency scan at $x = 0$ was fitted to the theory of equation (18) to obtain the following transport parameters: $\tau = 300$ μs, $D^* = 20$ cm^2 s^{-1}, $S_1 = 2100$ cm s^{-1} and $S_2 = 0.1$ cm s^{-1}. The frequency scans in the damaged region could not be fitted to

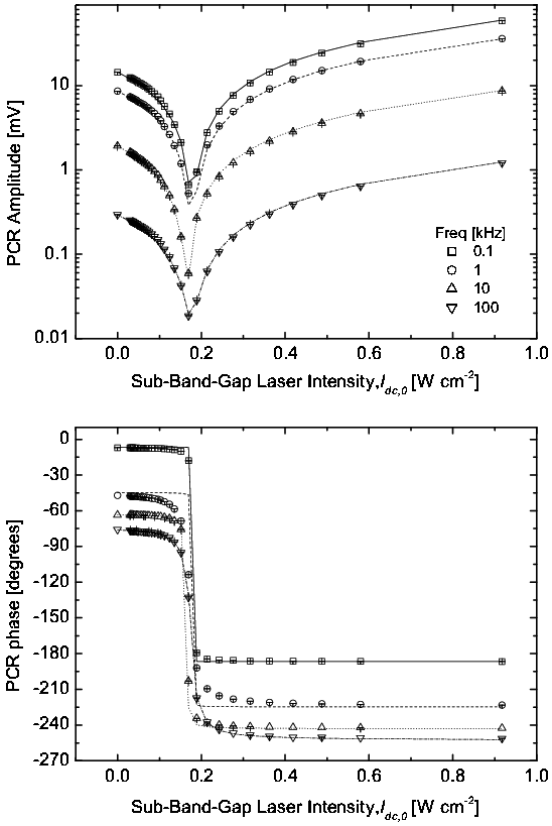

Figure 10. Experimental IR laser intensity scans (symbols) and best fits to theory (lines). The fitting results are shown in table 1.

theory, likely due to the inhomogeneity of the surface damage. IR laser intensity scans were performed at various positions along a line with $x = 0$ lying outside the damaged region, $x = 2.0$ mm lying at the centre of the damaged region (exhibiting the greatest degree of damage) and the damage level for intermediate locations scaling accordingly. The scans and fitting results are shown in figure 11. Simulations (figure 7) showed that the crossover position was not expected to change significantly with variations in the electronic integrity of the front surface so it was assumed that the shift of the experimental curves to lower IR laser powers for increasing damage must be due to changes in the radiative efficiency I_{eR}. Using the transport parameters from the $x = 0$ (undamaged) frequency scan fit, the instrumental factor ($\gamma = 716\,445$) was calculated from the $I_{dc,0} = 0$ amplitude in the manner discussed above assuming that $C(E) = 1.0 \times 10^{-20}$ cm^2 and $I_{eR} = 4.0 \times 10^{-3}$ W cm^{-2}. Fixing $C(E)$ and γ, the values of I_{eR} were found from the $I_{dc,0} = 0$ value of each remaining scan and the curves were fitted by adjusting the value of B. The FSRV values for the first two points were obtained from frequency scans that had a fitting error of $\sim$5%. For the remaining scans the FSRV were determined from several possible values from the relative drop of the $I_{dc,0} = 0$ amplitude and they are those that gave the minimum fitting error. No optical damage was accounted for with these fits. It has been assumed that changes in the optical reflectance had a small influence on both the number of generated carriers and the intensity of photo-emission, and so can be neglected in this exercise. While it may be possible to show that the curves can be fitted by incorporating optical

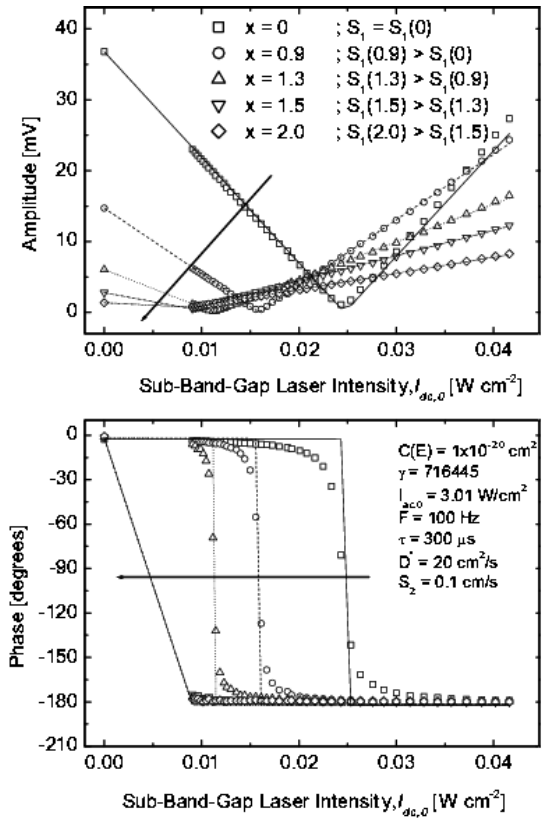

Figure 11. IR laser power scans (symbols) for increasingly damaged front surface (increasing recombination velocity) and best fits to theory (lines). Arrows indicate increasing damage level. The fitting results are shown in table 2.

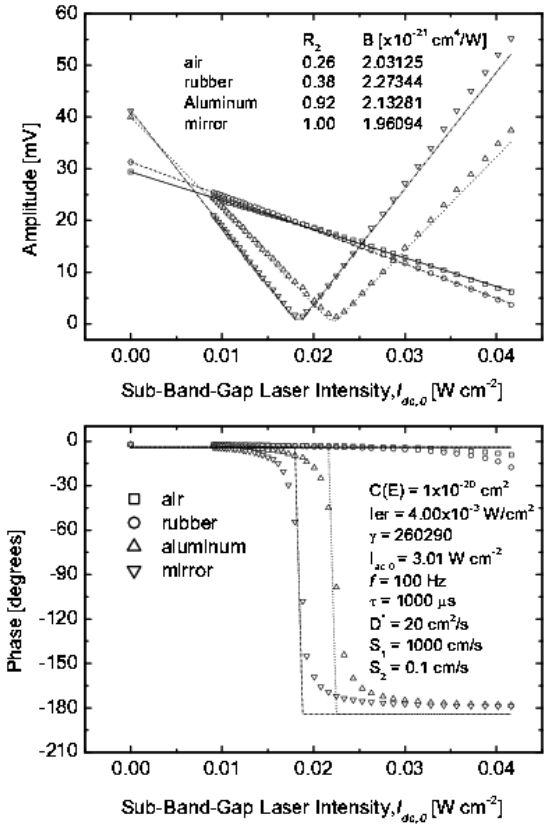

Figure 12. Experimental IR laser power scans (symbols) for different backing materials R_2 and best fits to theory (lines).

damage, the introduction of another variable would render the fit non-unique. With no predetermined value for the reflectance as a function of damage, which was undetectable by the human eye, these additional fits would provide little additional value. Simulations of the influence of R_{10} show that changes in the reflectance will affect the crossing point but that the $I_{dc,0} = 0$ amplitude increases with decreasing R_{10} whereas the presented experiments show a decreasing amplitude for increasing damage. This suggests that the electronic damage dominates any optical damage effects and variations in reflectance can be neglected. The values obtained from the fits are presented in table 2. The trends for surface-damage-dependent (increasing) FSRV, decreasing effective radiative emission intensity, I_{eR}, and essentially damage-independent constant B (a bulk optoelectronic parameter) are physically reasonable and expected. It is important to note that single-beam (conventional) PCR alone would not be able to yield quantitative values of the parameters I_{eR} and B: this can only be achieved by scanning the independently and accurately determined subband-gap beam intensity $I_{dc,0}$ through cross-modulation coupling to the PCR emissions.

The second set of experiments was designed to investigate the effect of the reflectance of the backing material supporting the wafer, which can be accounted for in the theory by the back surface reflectance, R_2. IR laser power scans were performed on an intact (non-damaged) region of the same wafer used for the front surface damage experiments with the wafer resting, respectively, on air, rubber, polished aluminium and a mirror.

Table 2. Fitting results for IR laser intensity scans of figure 11.

	Increasing surface damage severity				
x (mm)	0	0.9	1.3	1.5	2.0
S_1 (cm s^{-1})	2100	4700	10^4	5×10^4	10^6
B ($\times10^{-22}$ cm^4 W^{-1})	9.9305	6.6927	8.6208	3.0547	9.3120
I_{eR} ($\times10^{-3}$ W cm^{-2})	4.0000	2.9337	1.9384	1.6300	0.9921

The theoretical reflectance for a silicon–air interface varies as a function of wavelength in the near-IR: for $\lambda = 1550$ nm, $n = 3.478$ and $R = 0.306$; for $\lambda = 1120$ nm, $n = 3.536$ and $R = 0.313$ [36]. For all of the simulations and fits presented previously it was assumed that $R_{10} = R_2 = 0.320$. Using assumed transport parameters similar to those obtained for other regions of the wafer, the instrumental factor was obtained from the $I_{dc,0} = 0$ amplitude when the sample was over air assuming $C(E) = 1.0 \times 10^{-20}$ cm^2 and $I_{eR} = 4.0 \times 10^{-3}$ W cm^{-2} and the curve was then fitted with B left as a free variable. Assuming all values that contribute to the $I_{dc,0} = 0$ amplitude (namely $C(E)$, I_{eR}, γ and the transport parameters) were constant, the value of R_2 was increased to meet the $I_{dc,0} = 0$ amplitudes of the other curves. The initial value of $R_{2(air)} = 0.32$ did not allow for a sufficiently high amplitude for the curves with the sample resting on the mirror even with $R_{2(mirror)} = 1.0$. The results for the air and mirror were repeatedly fitted for decreasing $R_{2(air)}$ until all of the curves could be fitted. The fitting results are shown in figure 12, with the values of R_2 in the inset of figure 12(a).

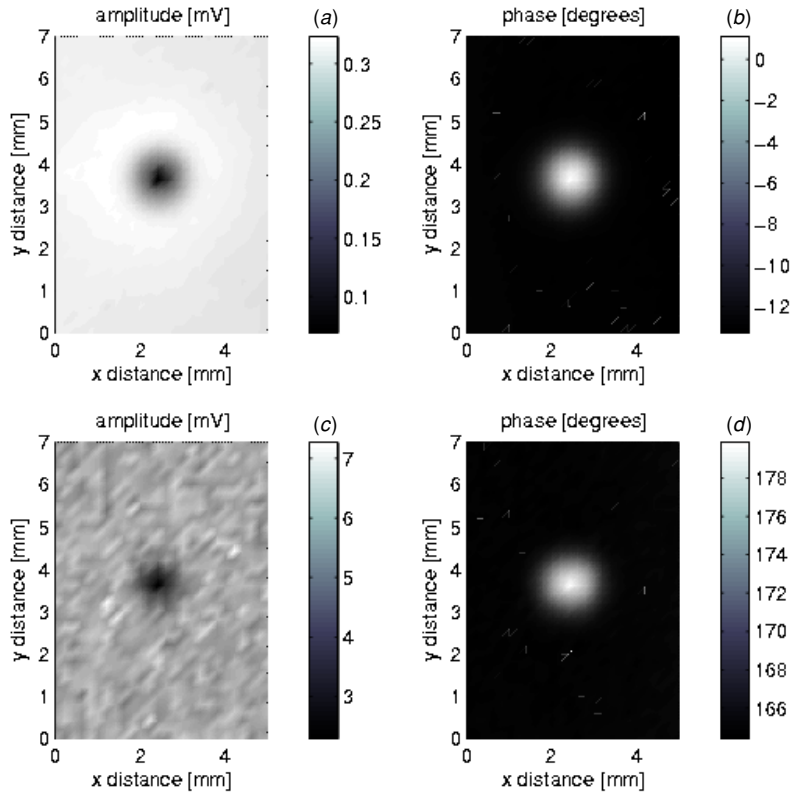

Figure 13. Lateral surface scans of iron contaminated silicon wafer at 10 kHz: conventional PCR ($I_{dc,0} = 0$) ((*a*) and (*b*)); and cross-modulated IR laser-dominated PCR ((*c*) and (*d*)).

Despite the fact that frequency scans were not performed at this location and the transport parameters have been estimated from previous fits of this wafer, the resulting fits using changes in only R_2 and B (which had only a minor variation between scans) are of good quality considering the approximations and further strengthen the validity of the model. It is possible that the lower $R_{2(air)}$ that was required to have a suitable $I_{dc,0} = 0$ amplitude range may be a result of multiple inter-reflections becoming more significant at very high R_2 (mirror and aluminium) and thus increasing the overall amplitude. Using the reflectance of the air–silicon interface the multiple passes were insignificant with respect to the first optical pass (so only the $n = 0$ term of equation (16) was used). Regarding the quality of the phase fits, figures 11(*b*) and 12(*b*), it should be noted that the IR laser power scans for the surface damage and backing material experiments were performed using a preliminary experimental geometry in which the two laser beams were not collinear and the IR beam was not focused. The curvature of the phase in the cross-over region is much larger than experimental results presented earlier in this paper or the curvature predicted by the theory for such low frequencies. It is likely that this curvature is related to the degree of overlap of the excess carrier density distribution and the volume that the IR laser probes (interaction volume) as it traverses the sample. Regardless, the fits of the front surface recombination velocity and the back surface reflectance curves demonstrate the validity of the one-dimensional model on a qualitative level, at the very least.

5. Imaging of electronic defects

The cross-modulation PCR technique has the clear advantage of quantitative determination of the interaction optoelectronic parameter B, as well as the radiative (recombination) emission intensity I_{eR}; these properties are in addition to the measurement of the electronic transport parameters for which conventional PCR has been proven capable. A full three-dimensional theory would, thus, be useful for a detailed study of the influence of a subband-gap light source on the occupation of defect/impurity states and the subsequent variation of the recombination parameters that could be carried out by fitting frequency scans for various IR laser intensities. Furthermore, the introduction of the IR dc beam has a potential value as a resolution and contrast enhancement agent for free-carrier density imaging applications [21]. The ability to scale the signal amplitude through cross-modulation with the subband-gap laser power provides a method of signal amplification that will result in higher signal-to-noise ratios and allow imaging at lower superband-gap intensities than possible with conventional PCR.

Two-beam cross-modulation PCR images of an iron contaminated region in a p-type Si wafer are shown in figure 13 operating in the radiative emission dominated regime ((*a*) and (*b*)) and in the cross-modulated IR laser dominated regime ((*c*) and (*d*)). The amplitude image in the IR laser dominated regime (*c*) has a poorer contrast than the conventional PCR image (*a*) due to superposition of an image of the residual optical properties of the sample, especially the

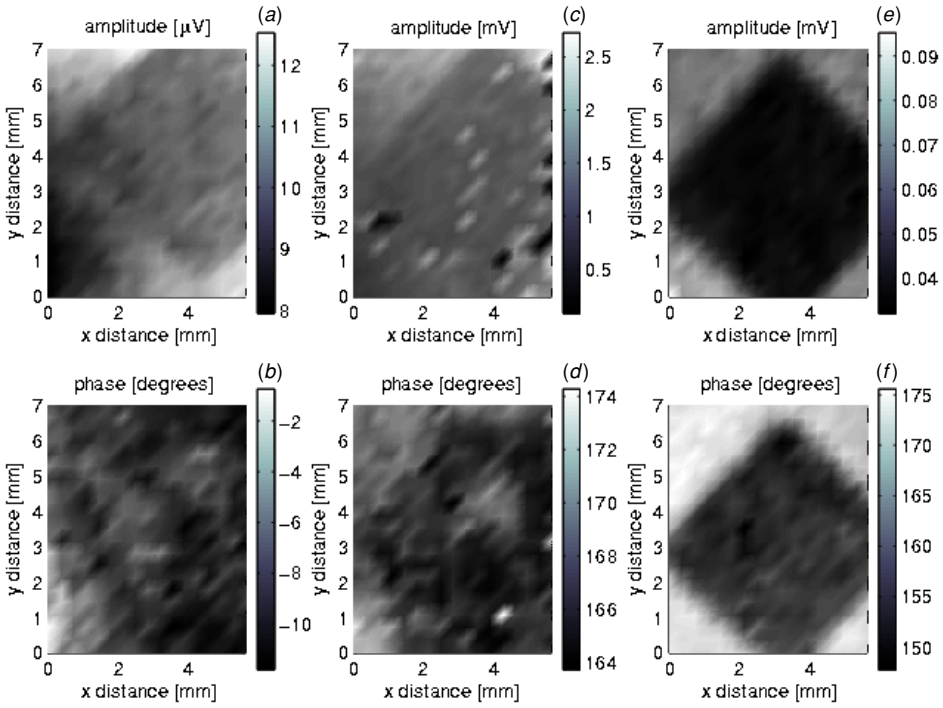

Figure 14. Conventional PCR images of H^+ implanted into oxidized p-type Cz–Si wafer (0.75 MeV, 3×10^{14} cm^{-2}) performed at 10 kHz and $P_{ac} = 19$ mW ((*a*) and (*b*)). Two-beam cross-modulated PCR scans of same diamond shaped feature operating in the IR laser dominated regime ($P_{dc} = 1.65$ mW) for different ac power levels: 19 mW ((*c*) and (*d*)) and 1.15 mW ((*e*) and (*f*)).

microscopic roughness of the back surface. The source of these new features was determined by scanning the sample with the IR laser chopped at 600 Hz and the superband-gap laser turned off. The results clearly showed the same background features that were introduced in figure 13(*c*) without the contamination image. The phase image (*d*) does not contain the background artefacts because phase, as the ratio of the quadrature and in-phase signals, both of which are proportional to the product $I_{ac,0}\, I_{dc,0}$ under cross-modulation, is not affected by variations in the intensity of either the superband-gap or the subband-gap beam. The phase contrast for the contamination region is thus similar to the contrast using conventional PCR image (*b*). The benefits of using the cross-modulation configuration become apparent when comparing the signal-to-noise ratios (SNR) of the two techniques. Despite any noise introduced by the presence of a second laser beam, the average SNR of the data points comprising the cross-modulated image is 122% greater than the average for the conventional PCR image. This technique allows the power of the superband-gap laser to be reduced while maintaining sufficiently high SNRs and thus provides a methodology for imaging at lower injection levels than other optical techniques, including conventional PCR.

The aforementioned imaging advantages obtained by introducing the subband-gap laser beam were demonstrated using H^+ implanted p-type Cz–Si with a thermally grown oxide. Diamond shaped regions with sides approximately 5 mm long were implanted with energy ranging from 0.75 MeV to 2 MeV and dose ranging from 3×10^{14} to 3×10^{16} cm^{-2}. The benefits of working at low injection levels become evident when examining the images of the sample that had undergone the least amount of damage to the crystalline structure (0.75 MeV, 3×10^{14} cm^{-2}). A portion of the diamond is slightly visible in the upper right region of the conventional amplitude and phase PCR images (figures 14(*a*) and (*b*)) and the cross-modulation scans using the identical superband-gap power of 19 mW (figures 14(*c*) and (*d*)). Imaging at other modulation frequencies produced similarly poor results. This is likely due to electronic trap-filling saturation by the photo-exciting laser. Decreasing the superband-gap power to 1.15 mW, and thus lowering the injected carrier density by more than an order of magnitude, dramatically improved the image contrast in both amplitude and phase (figures 14(*e*) and (*f*)). The sample was moved between scans resulting in the diamond being located at different coordinates for each IR laser power setting. It is concluded that lower injection levels enhance electronic damage contrast by trap-filling below the saturation levels, thus optimally delineating the sub-surface defect structure. The samples implanted with high dose and/or higher energy had significantly greater amount of damage to the crystal structure and showed good image contrast in the amplitude using conventional PCR, especially at low frequencies, but the phase contrast was very poor to non-existent. For this higher degree of damage the introduction of the IR laser beam was seen to drastically enhance the imaging resolution with no need for lowering the injection level. The use of a cross-modulation geometry also appears to decrease the diffusion dependence of imaging resolution compared to conventional PCR [17]. The damage introduced by the implantation process will reduce the average carrier lifetime and may be sufficient to increase the optical absorption coefficient in the near surface region. These modifications cause a shift in the dominant recombination mechanism and a resulting phase contrast of greater than 180°.

6. Conclusions

A modification of conventional PCR incorporating a secondary subband-gap infrared laser has been developed to utilize the superposition of the recombination induced radiative emissions and the cross-modulated backscattered IR laser intensity resulting from the carrier-wave dependent harmonic infrared absorption coefficient. Various configurations of this two-beam cross-modulation approach have been applied to the imaging of electronic contamination and defects in silicon wafers and a one-dimensional theory was developed to explain the experimental dependence of electronic transport properties on the intensity of the subband-gap beam. Cross-modulation PCR was shown to yield, for the first time, quantitative values of the optoelectronic constant B associated with the change of free-carrier capture cross-section in the presence of band-to-band optical absorption, as well as of I_{eR}, the intensity of radiative recombination emissions. These values cannot be measured by conventional PCR or other single-ended optoelectronic techniques. The two-beam cross-modulation PCR was further shown to enhance the imaging contrast of a certain electronic contamination type (Fe in p-Si) and subsurface defects. The technique was shown to yield dramatic phase contrast enhancement at superband-gap laser intensity levels untenably low ($\sim$1.15 mW) for single-ended PCR and other optoelectronic imaging methodologies [26, 33], tentatively attributed to relatively low-injection trap-filling below opto-electronic trap saturation.

Acknowledgments

The authors wish to thank the Natural Sciences and Engineering Research Council of Canada (NSERC) and Materials and Manufacturing Ontario (MMO) for support of this research.

References

[1] Fan H Y and Becker M 1951 *Semiconducting Materials* (London: Butterworth) p 132
[2] Visvanathan S 1960 *Phys. Rev.* **120** 376
[3] Fan H Y, Spitzer W G and Collins R J 1956 *Phys. Rev.* **101** 566
[4] Pankove J I 1971 *Optical Processes in Semiconductors* (New York: Dover) pp 74–5
[5] Schroder D K, Thomas R N and Swartz J C 1978 *IEEE J. Solid-State Circuits* **31** 180
[6] Smith R A 1978 *Semiconductors* 2nd edn (Cambridge: Cambridge University Press) pp 294–300
[7] Hara H and Nishi Y 1966 *J. Phys. Soc. Japan* **21** 1222
[8] Spitzer W and Fan H Y 1957 *Phys. Rev.* **108** 268
[9] Soref R A and Bennett B R 1987 *IEEE J. Quantum Electron.* **23** 123
[10] Koskowich G N, Darling R B and Soma M 1988 *Phys. Rev.* B **38** 1281
[11] Mroczkowski J A, Shanley J F, Reine M B, LoVecchio P and Polla D L 1981 *Appl. Phys. Lett.* **38** 261
[12] Kirkpatrick C G, Noonan J R and Streetman B G 1976 *Radiat. Effects* **30** 97
[13] Nakashima H, Shiraki Y and Miyao M 1979 *J. Appl. Phys.* **50** 5966
[14] Pankove J I and Wu C P 1979 *Appl. Phys. Lett.* **35** 937
[15] Shockley W and Read W T 1952 *Phys. Rev.* **87** 835
[16] Kirchhoff G 1898 *Abhandlungen über Emission und Absorption* ed M Planck (Leipsig: Verlag von Wilhelm Engellman) pp 11–36
[17] Mandelis A, Batista J and Shaughnessy D 2003 *Phys. Rev.* B **67** 205208
[18] King O and Hall D G 1994-I *Phys. Rev.* B **50** 10661
[19] Guidotti D, Batchelder J S, Van Vechten J A and Finkel A 1986 *Appl. Phys. Lett.* **48** 68
[20] Kurner W, Sauer R, Dornen A and Thonke K 1989 *Phys. Rev.* B **39** 13327
[21] Batista J, Mandelis A and Shaughnessy D 2003 *Appl. Phys. Lett.* **82** 4077
[22] Guidotti D, Batchelder J S, Finkel A and Van Vechten J A 1988-I *Phys. Rev.* B **38** 1569
Guidotti D, Batchelder J S, Finkel A, Gerber P D and Van Vechten J A 1989 *J. Appl. Phys.* **66** 2542
[23] Mandelis A 2001 *Diffusion-Wave Fields: Mathematical Methods and Green Functions* (New York: Springer) chapter 9
[24] Mandelis A 2005 *J. Appl. Phys.* **97** 083508
[25] Batista J, Mandelis A, Shaughnessy D and Li B 2004 *Appl. Phys. Lett.* **85** 1713
[26] Mandelis A 1998 *Solid-State Electron.* **42** 1
[27] Bauda P F, Tamagawa T and Polla D L 1990 *Appl. Phys. Lett.* **57** 2579
[28] Sanii F, Giles F P, Schwartz R J and Gray J L 1992 *Solid-State Electron.* **35** 311
[29] Mandelis A, Pawlak M and Shaughnessy D 2004 *Semicond. Sci. Technol.* **19** 1240
[30] Opsal J, Taylor M W, Smith W L and Rosencwaig A 1986 *J. Appl. Phys.* **61** 240
[31] Born M and Wolf E 1980 *Principles of Optics* 6th edn (Oxford: Pergamon) chapters 1, 7, 13
[32] Wagner R E 1994 Quantitative photomodulated optical-reflectance studies of silicon and germanium semiconductors *PhD Thesis* University of Toronto
[33] Schroder D K 1998 *Semiconductor Material and Device Characterization* 2nd edn (Wiley: New York) chapter 7, pp 439–48
[34] Luke K L and Cheng L-J 1987 *J. Appl. Phys.* **61** 2282
[35] Schroder D K, Thomas R N and Swartz J C 1978 *IEEE Trans. Electron. Dev.* **25** 294
[36] Edwards D F 1998 Silicon (SI) *Handbook of Optical Constants of Solids* ed E D Palik (Academic: New York)